

Iodine-filter-based mobile Doppler lidar to make continuous and full-azimuth-scanned wind measurements: data acquisition and analysis system, data retrieval methods, and error analysis

Zhangjun Wang,^{1,3,*} Zhishen Liu,¹ Liping Liu,² Songhua Wu,¹
Bingyi Liu,¹ Zhigang Li,¹ and Xinzhao Chu³

¹Ocean Remote Sensing Institute, Ocean University of China, 5 Yushan Road, Qingdao 266003, China

²State Key Laboratory of Severe Weather, Chinese Academy of Meteorological Sciences, China Meteorology Administration, 46 Zhongguancun Nanda Street, Beijing 100081, China

³Cooperative Institute for Research in Environmental Sciences & Department of Aerospace Engineering Sciences, University of Colorado at Boulder, 216 UCB, Boulder, Colorado 80309, USA

*Corresponding author: zhangjun.wang@colorado.edu

Received 23 March 2010; revised 27 October 2010; accepted 7 November 2010;
posted 9 November 2010 (Doc. ID 125867); published 17 December 2010

An incoherent Doppler wind lidar based on iodine edge filters has been developed at the Ocean University of China for remote measurements of atmospheric wind fields. The lidar is compact enough to fit in a minivan for mobile deployment. With its sophisticated and user-friendly data acquisition and analysis system (DAAS), this lidar has made a variety of line-of-sight (LOS) wind measurements in different operational modes. Through carefully developed data retrieval procedures, various wind products are provided by the lidar, including wind profile, LOS wind velocities in plan position indicator (PPI) and range height indicator (RHI) modes, and sea surface wind. Data are processed and displayed in real time, and continuous wind measurements have been demonstrated for as many as 16 days. Full-azimuth-scanned wind measurements in PPI mode and full-elevation-scanned wind measurements in RHI mode have been achieved with this lidar. The detection range of LOS wind velocity PPI and RHI reaches 8–10 km at night and 6–8 km during daytime with range resolution of 10 m and temporal resolution of 3 min. In this paper, we introduce the DAAS architecture and describe the data retrieval methods for various operation modes. We present the measurement procedures and results of LOS wind velocities in PPI and RHI scans along with wind profiles obtained by Doppler beam swing. The sea surface wind measured for the sailing competition during the 2008 Beijing Olympics is also presented. The precision and accuracy of wind measurements are estimated through analysis of the random errors associated with photon noise and the systematic errors introduced by the assumptions made in data retrieval. The three assumptions of horizontal homogeneity of atmosphere, close-to-zero vertical wind, and uniform sensitivity are made in order to experimentally determine the zero wind ratio and the measurement sensitivity, which are important factors in LOS wind retrieval. Deviations may occur under certain meteorological conditions, leading to bias in these situations. Based on the error analyses and measurement results, we point out the application ranges of this Doppler lidar and propose several paths for future improvement. © 2010 Optical Society of America

OCIS codes: 280.3640, 170.3340, 300.6320.

1. Introduction

Wind is one of the most important variables in atmospheric dynamics, and it is crucial to weather forecasting using numerical models. It is also key to studying atmospheric coupling and transport. Wind measurements are important to many other applications like aviation control, sea surface wind monitoring, space shuttle launch and landing, etc. Doppler wind lidars have demonstrated their efficacy in wind measurements where spatially- and range-resolved measurements of wind velocity are needed.

Both coherent-detection and direct-detection Doppler lidars have been developed for wind measurements. The NOAA Environmental Technology Lab developed a scanning coherent Doppler lidar based on a pulsed $10.6\ \mu\text{m}$ CO_2 laser in the 1980s [1]. This lidar was operated with a circular scanner at a rate of $3.3^\circ/\text{s}$ and at a constant elevation angle of 0.5° for numerous field campaigns of wind measurements [2]. NOAA's High-Resolution Doppler Lidar (HRDL) [3] was developed for measuring the mean and turbulent velocity structure of the atmospheric boundary layer. This lidar is normally mounted in a seatainer and has been operated in ground-based and shipborne field experiments. Coherent Doppler lidars have been employed to measure the boundary-layer mixing height, sea breeze, downslope windstorms, and flow in complex terrain in the near-horizontal scan mode over the past 25 years [4].

Compared to coherent Doppler lidars that rely on aerosol backscatter signals, and thus are limited to lower atmosphere where aerosols are abundant, incoherent direct-detection Doppler lidars that can exploit both aerosol and molecular backscatter signals as well as atomic resonance fluorescence cover a much larger altitude range, to as high as 110 km with resonance-fluorescence Doppler lidars [5], or from near ground to ~ 60 km with Rayleigh/Mie Doppler lidars [6–20]. However, the near-horizontal scan is a challenging task for incoherent lidars. Instead of employing optical heterodyne detection technology to infer wind-induced Doppler shift in coherent lidars, direct-detection Doppler lidars convert the Doppler shift into a change in received light power or power ratio using various optical frequency discriminators. These discriminators include Fabry–Perot interferometer, Fizeau etalon, iodine vapor cell filter, Na vapor cell filter, etc., implemented in lidar receiver chains. Metal atoms such as Na, Fe, and K in the mesosphere and lower thermosphere provide natural frequency discriminators with their absorption lines [5]. In 1989, the Service d'Aeronomie of National Center for Scientific Research (CNRS) in France demonstrated a ground-based Rayleigh Doppler lidar using a frequency-doubled Nd:YAG laser and double-edge filter made of a dual Fabry–Perot interferometer for measurements of wind profiles between 25 km and 60 km [6]. Later, the GLOW (Goddard Lidar Observatory for Winds) mobile direct-detection Doppler lidar was developed by researchers at the NASA/Goddard Space Flight Center in the U.S.A. It measures wind

from aerosol scattering at 1064 nm and from molecular scattering at 355 nm, each using a double-edge Fabry–Perot interferometer. The 355 nm system measures wind profiles up to 35 km altitude [7]. In 1997, a high-resolution incoherent Doppler lidar using “full fringe imaging” was constructed at the Space Physics Research Laboratory at the University of Michigan [8]. The ADM-Aeolus Atmospheric Laser Doppler Instrument (ALADIN) will employ an aerosol channel using a Fizeau interferometer and a molecular channel using a Fabry–Perot etalon [9]. A multibeam Fizeau interferometer combined with a linear detector as a spectral analyzer has been proposed by McKay [10]. A direct-detection Doppler lidar utilizing a multibeam Fizeau interferometer was developed in the Shanghai Institute of Optics and Fine Mechanics in 2005 for planetary boundary-layer wind field measurement [11]. At the same time, the University of Geneva [12] was involved in the further development and exploitation of the direct-detection lidar (DDL) double-edge technique.

Resonance-fluorescence Doppler lidar is another type of direct-detection Doppler lidar [5], which can monitor temperature and wind in the mesosphere and lower thermosphere (75–110 km) where the atmospheric density and aerosol concentration are far too low for molecular or aerosol signals to be used for wind measurements. The beauty of this lidar is its nature-provided frequency discriminator in the atmosphere—the atomic absorption lines of Fe, Na, and K atoms that are Doppler shifted and broadened so that they can be used to infer atmosphere temperature and wind; thus, the lidar receiver is broadband for maximum return signals. Recently, Huang *et al.* [13] proposed a Na double-edge magneto-optic filter (Na-DEMOF) to extend Na Doppler lidar measurements via Rayleigh-Mie scattering into the lower atmosphere. Field campaigns demonstrated wind and temperature profiling in the altitude range of 10–45 km with 1 km resolution and 60 min integration [14].

In 1997, Friedman *et al.* [15], building on the work of Tepley *et al.* [16], demonstrated wind measurements in the stratosphere and lower mesosphere using a Rayleigh Doppler lidar based on an iodine edge filter at Arecibo Observatory. Wind profiles were obtained from 18 to 45 km with 1.5 km range resolution neglecting the influence of Mie scattering. Around the same time, Liu *et al.* [17] proposed using an iodine edge filter for frequency analysis of the backscattered light from both atmospheric molecules and aerosols for lower atmosphere wind measurements. The iodine-filter-based Doppler lidar has two advantages in this application. First, such a molecular filter has absolute frequency calibration and is repeatable from day to day and from location to location, in contrast to an etalon system. Second, this filter has an absorption line at 532 nm, reachable by frequency-doubled Nd:YAG laser. The Nd:YAG laser has reached mature status with high power, single mode, and single frequency. Diode-laser pumping

has further made it robust and reliable, with a high repetition rate. Therefore, iodine-filter-based direct-detection Doppler lidars are expected to have large power-aperture product and reliable performance.

Based on the proposal by Liu *et al.* [17], a mobile Doppler wind lidar was developed at the Ocean University of China for boundary-layer and troposphere wind measurements [18,21]. This iodine-filter-based lidar is capable of scanning measurements of three-dimensional wind field in real time. The lidar system is compact and integrated into a minivan. Numerous observational campaigns have been made with this lidar for sea surface, boundary-layer, and troposphere wind measurements [22,23]. It is noteworthy that continuous measurements of sea surface wind were made for 16 days during the 2008 Beijing Olympic Games in support of the sailing competition in Qingdao, China.

In this paper, we briefly introduce the lidar instrumentation (Section 2) and then present the data acquisition and analysis system (DAAS) (Section 3) developed for the mobile Doppler wind lidar. An attractive feature of this lidar and its DAAS is its capability of handling a variety of measurements, such as wind profile, line-of-sight (LOS) wind velocity in plan position indicator (PPI) and range height indicator (RHI) modes, sea surface wind (SSW), horizontal visibility, and aerosol backscattering ratio in different

operation modes, while processing data and displaying retrieved results in real time. This paper will introduce the data retrieval methods and discuss the assumptions made in each case (Subsection 4.A), and then analyze the measurement errors introduced by photon noise and several assumptions (Subsection 4.B). We also present the measurement procedures and results for wind profiles (Subsection 5.A), LOS wind velocities in PPI and RHI modes (Subsections 5.B and 5.C), along with SSWs measured for the 2008 Beijing Olympics (Subsection 5.D). Finally, in Section 6 we conclude the paper by pointing out the application ranges of this Doppler lidar and propose a few ideas for future improvement.

2. Doppler Wind Lidar Instrumentation

Figure 1 is a schematic diagram of the mobile incoherent Doppler wind lidar. The entire system comprises three major function blocks: the lidar transmitter, the lidar receiver, and the data acquisition and analysis system. An add-on two-axis scanner with 32 cm diameter aperture is unique to this lidar as it provides the full-azimuth and full-elevation scanning capability. The lidar transmitter provides high-repetition-rate and frequency-stabilized laser pulses at 532 nm by a diode-pumped, frequency-doubled, pulsed Nd:YAG laser, injection seeded by a continuous wave (CW) seed laser and stabilized to an iodine absorption

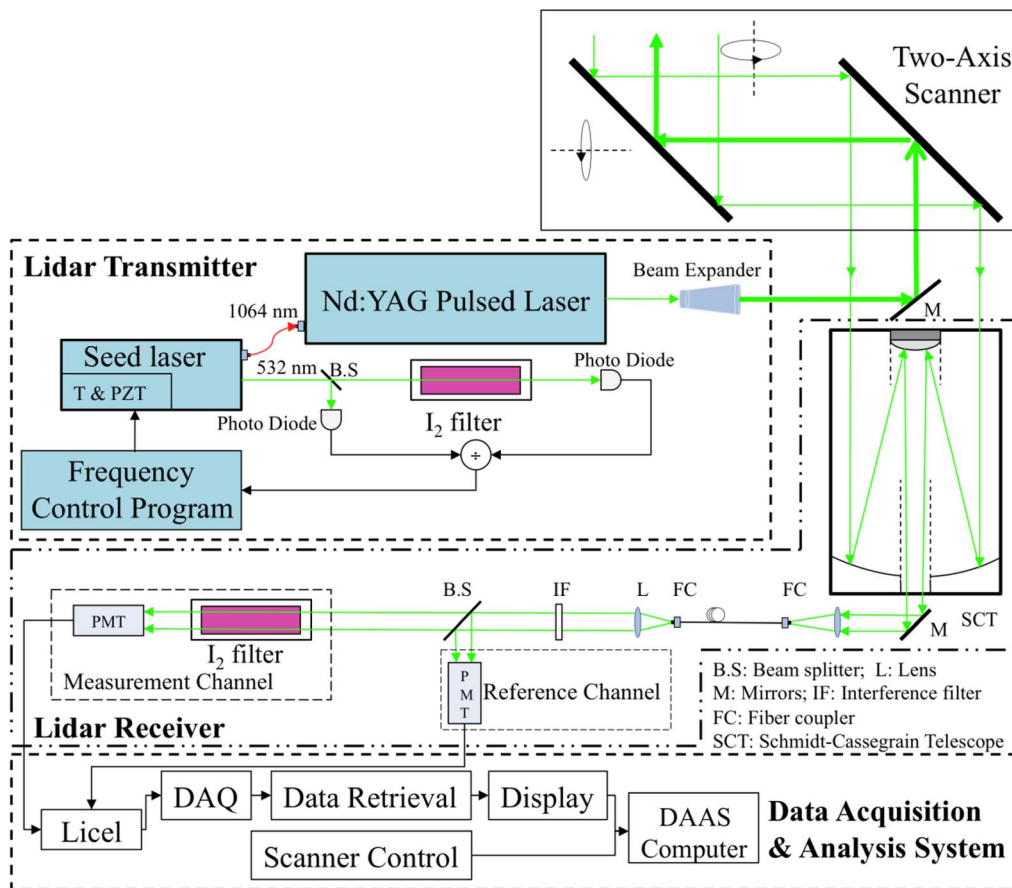


Fig. 1. (Color online) Schematic diagram of the incoherent mobile and scanning Doppler wind lidar.

line [24,25]. The laser repetition rate is 2.8 kHz, and the single pulse energy is ~ 2 mJ with pulse width of 30 ns. The seed laser is a CW Nd:YAG laser and it has dual outputs: the 1064 nm laser is injected into the pulsed Nd:YAG laser while the frequency-doubled laser at 532 nm is locked to the 50% absorption level of the I_2 line 1109 to stabilize the seed laser frequency. The frequency stability of the seed and pulsed Nd:YAG lasers are 200 kHz and 1 MHz, respectively. The spectral linewidth of the laser pulses is within 35 MHz. The outgoing laser beam is expanded to 70 μ rad divergence by a 20 \times beam expander, and then directed into the sky via a steering mirror coaxial with the scanner. The two-axis scanner provides coverage over an entire hemisphere ($0^\circ - 360^\circ$ azimuth and $0^\circ - 180^\circ$ elevation). This scanner can accommodate coaxial transmission and reception with continuous scanning speed of $1^\circ - 10^\circ/s$ and directional accuracy of 0.1° . It enables the scanning measurements with high spatial and temporal resolutions.

The lidar receiver is based on the iodine edge-filter technique [17], and the iodine absorption line 1109 is chosen as the frequency discriminator. A 30.5 cm diameter Schmidt-Cassegrain telescope with a field of view of 120 μ rad is employed to collect backscattered photons. The return signals collected by the telescope are coupled through a fiber and pass through an interference filter. This filter is centered at 532 nm with a passband of 0.11 nm and a peak transmission of 76%. The signals are then split into two channels: one is detected directly by a photomultiplier tube (PMT) as a reference channel, and another goes

through an iodine filter before being detected by another PMT in the measurement channel. Acquisition of both channels of data is handled by the data acquisition and analysis system (DAAS). To cover the huge and variable dynamic ranges of backscatter signals from the troposphere, a multichannel scaler (MCS) device, manufactured by Licel, is operated in both photon counting and analog modes to receive the PMT signals from both channels. The DAAS then processes the data in real time with 10 m resolution for the altitude range from 0 m to 20 km to retrieve wind products. The DAAS also controls the two-axis scanner and displays the retrieved winds in real time.

There are three key components for continuous and full-azimuth-scanned wind measurements: the transmitter with a high-power and high-repetition-rate laser, the receiver with a well-calibrated iodine edge filter, and the user-friendly data acquisition and analysis system (DAAS) that includes a two-axis scanner. The focus of this paper is the DAAS and the data retrieval principles and error analyses behind the DAAS.

3. Architecture of Data Acquisition and Analysis System

As laid out in Fig. 2, the overall computer-control system of the Doppler wind lidar is comprised of two major programs: the laser frequency control program and the data acquisition and analysis system (DAAS). The frequency-locking module, developed in the National Instrument LabVIEW program, is

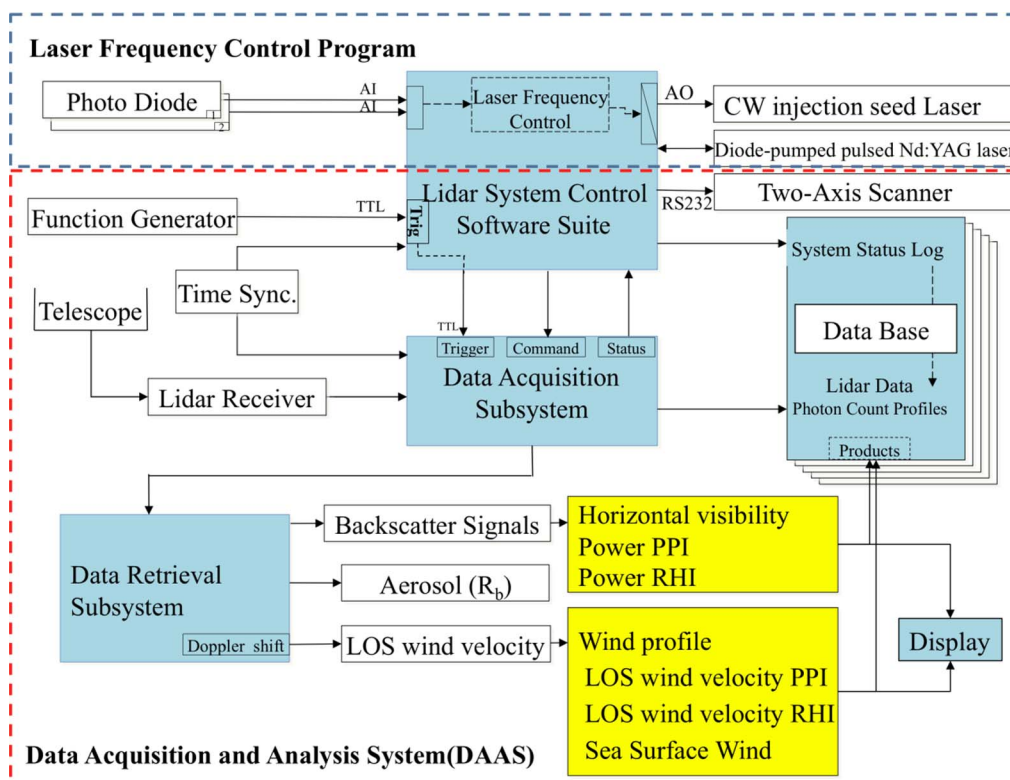


Fig. 2. (Color online) Architecture of the overall computer control system for the mobile Doppler wind lidar.

used to stabilize the seed laser frequency to the desired points on the I_2 absorption line number 1109. It can also be adapted to lock the pulsed laser frequency directly to the I_2 line. Details about this program can be found in Refs. [24,25] so they are omitted from this paper. The DAAS consists of five function modules: a two-axis scanner control program, a data acquisition (DAQ) subsystem, a data storage subsystem, a data retrieval subsystem, and a display module. As part of the “Lidar System Control Software Suite,” the scanner control program controls both azimuth and elevation scans, and monitors the scanner’s status. A function generator is used to provide the time synchronization between the transmitter laser and the data acquisition subsystem. This DAQ subsystem works with the Licel MCS device to detect the return photons in both photon counting and analog modes, and then accumulates the signals for a set number of laser shots before it writes the raw data profiles into the data storage area. In addition to storing the raw lidar data in both ASCII and binary formats, the data storage subsystem also saves the lidar system parameters provided by the control software suite and the retrieval products provided by the data retrieval program. The data retrieval is performed in real time, and as such, provides users with great flexibility. It can derive all possible data products including retrieval of backscatter signals to further derive horizontal visibility, retrieval of the aerosol backscatter ratio, and retrieval of the LOS wind velocity from the measured Doppler shift. Depending on operating modes, the LOS wind can be further turned into various products like wind-altitude profiles, LOS wind velocity PPI, LOS wind velocity RHI, and sea surface wind, etc. All these retrieval products can be illustrated in the display module depending on users’ choices.

The entire DAAS code was written in a combination of C and C++ under Microsoft Visual C++ 6.0 and OpenGL. Figure 3 shows the DAAS user interface with raw backscatter photon profiles for the measurement (lower profile) and reference (upper profile) channels displayed. The interface includes the wind profile controller pair, PPI controller pair, RHI controller pair, scanner controller pair, backscattered signal controller pair, and SSW controller pair for operation in different scanning modes. The monitor unit of the DAAS serves as a display module for all products and operation parameters. Here all the peripherals are controlled and system parameters are kept in ASCII and Binary files. This interface was designed to hide as much of the complexity as possible while giving the user a clean but still informative display. The lidar system has been deployed in many field campaigns [22,23] and the DAAS allows hands-off operation for many days. It can be handled easily and efficiently.

The DAQ subsystem is built around the Licel MCS Ethernet controller. Its Ethernet-based modules pave the way for truly remotely controlled experiments. These use a TCP/IP-based protocol with syn-

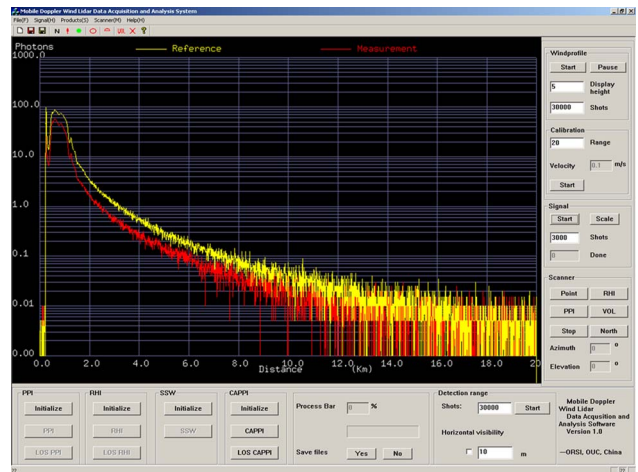


Fig. 3. (Color online) DAAS user interface with raw lidar data profiles and various control modules displayed.

tax similar to conventional GPIB-based instruments. The Licel MCS transient recorder systems have parallel analog and photon-counting detection chains. The combination of the two signals gives the high linearity of the analog signal for strong signals and the high sensitivity of the photon counting for weak optical signals. The integration of both detection mechanisms into a single device avoids ground loops and other problems that make the combination otherwise cumbersome [26].

A flowchart of the DAQ program is plotted in Fig. 4. When starting a data acquisition session, the user can choose between analog and photon-counting signals, to be displayed in linear or logarithmic coordinates. Users can also zoom in or out to see the details or entire profiles. DAAS, built around a multi-channel environment, can collect and display the backscatter signals in real time. The format for data saving was designed based on the characteristics of lidar data. The data include the raw signals, radial velocity, elevation, azimuth, time, laser repetition rate, and other key parameters.

4. Data Retrieval Methods and Error Analysis

As the Doppler lidar measures the LOS wind velocity, the lidar must be pointed zenith and then off-zenith in order to obtain the wind vector, which are primarily the horizontal wind components. In this way, the horizontal wind produces a LOS projection to the lidar beam, and with appropriate scanning schemes, the three-dimensional wind vector can be inferred. A necessary assumption is the horizontal homogeneity of the atmosphere (wind and temperature fields as well as aerosol distributions) over the scanned volume and during the time of integration. Vertical homogeneity is not required [27]. Such assumption of spatial uniformity has been a common practice for other Doppler lidars [28].

A. Data Retrieval Methods

The LOS wind velocity V_{LOS} is the sum of wind components produced by the horizontal and vertical

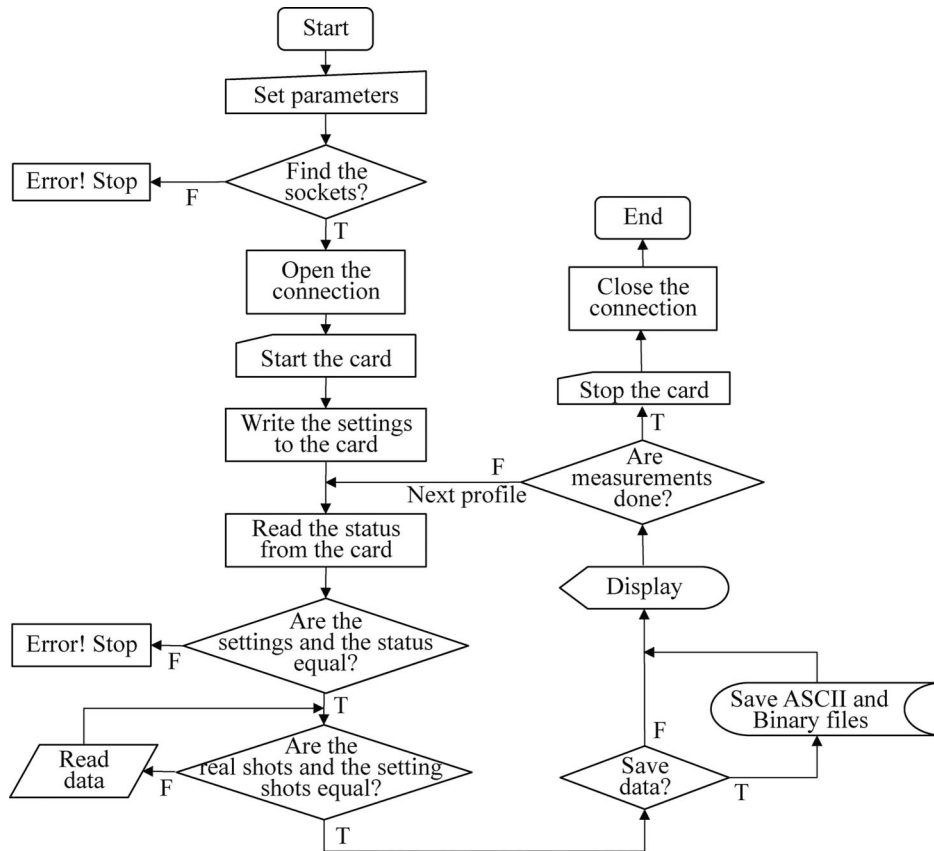


Fig. 4. Flowchart of the DAQ subsystem.

winds along the lidar beam direction. Thus, the total LOS wind velocity is given by

$$V_{\text{LOS}} = 0 + V_{\text{LOS},H} + V_{\text{LOS},V}, \quad (1)$$

where 0 represents zero LOS wind, $V_{\text{LOS},H}$ and $V_{\text{LOS},V}$ are the horizontal and vertical wind components to the LOS direction. Positive LOS wind velocity is defined as radially outward from the lidar. We define $R_{W,i}$ as the wind ratio of signal photon counts of the measurement channel to the reference channel in the i th (azimuth) LOS direction, which contains the information of Doppler shift. Using a linear approximation that the wind ratio after normalization to the zero-wind ratio is linearly proportional to the LOS wind velocity, we can express the overall wind ratio $R_{W,i}$ by

$$R_{W,i} = R_0 - \Delta R_{H,i} - \Delta R_{V,i}, \quad (2)$$

where R_0 is the zero-wind ratio corresponding to the “0” written in Eq. (1), i.e., the ratio of the measurement channel to the reference channel when the LOS wind velocity is zero, and $\Delta R_{H,i}$ and $\Delta R_{V,i}$ are the wind ratio changes caused by the horizontal and vertical wind components in the i th LOS direction, respectively. This linear approximation is a good first-order approximation to the reality, as demonstrated in Fig. 3 of [18] where a good linearity exists

between the normalized wind ratio and the LOS wind velocity in the range between ± 50 m/s. Such linearity was also assumed by other groups [15].

Under such linear approximation, we have the relationship

$$\Delta V_{\text{LOS}} = \frac{dV_{\text{LOS}}}{dR_W} \Delta R_W, \quad (3)$$

where $\Delta V_{\text{LOS}} = V_{\text{LOS}} - 0$ and $\Delta R_W = R_W - R_0$. Therefore, the LOS wind velocity can be calculated from the measured wind ratios using

$$V_{\text{LOS},i} = \frac{R_{W,i} - R_0}{R_0 S}, \quad (4)$$

where $R_{W,i}/R_0$ is the normalized wind ratio as defined in [18], and S is the wind measurement sensitivity. The sensitivity S is defined as the fractional change in the wind ratio per unit change in LOS wind velocity

$$S = \frac{1}{R_0} \frac{dR_W}{dV_{\text{LOS}}} = 3.76^* \frac{1}{R_0} \frac{dR_W}{d\nu}, \quad (5)$$

where ν is the laser frequency and $3.76 \text{ MHz}/(\text{m/s})$ is the Doppler shift of backscattered light caused by 1 m/s LOS wind velocity, which is given by $2/\lambda = 2/532 \text{ nm}$. Here $\lambda = 532 \text{ nm}$ is the outgoing laser wavelength. Therefore, after S is derived from

the experimentally measured $\frac{dR_W}{d\nu}$ and R_0 , we can calculate the LOS wind velocity as follows:

$$V_{\text{LOS},i} = \frac{R_{W,i} - R_0}{3.76^* dR_W/d\nu}. \quad (6)$$

Equation (6) is the basic relationship used in the derivation of the LOS wind velocity. Besides the measured wind ratio $R_{W,i}$, the fidelity of this data retrieval method relies on how well the two parameters R_0 and $dR_W/d\nu$ can be determined experimentally. To do so, two assumptions are further made in addition to the spatial homogeneity assumption mentioned earlier. First, the vertical wind assumption—the vertical wind averaged over sufficient periods is close to zero. Second, the uniform sensitivity assumption—the slope $dR_W/d\nu$ remains constant from the zenith to the off-zenith directions within a short measurement period and over a small scanned volume. Any deviation of the assumptions from the actual atmosphere conditions will lead to systematic errors in the retrieved LOS wind. The error analysis provided in Subsection 4.B will impose limitations on the applicable range of this Doppler lidar with current retrieval methods.

In practice, the sensitivity S is measured in the zenith direction with the Nd:YAG laser tuned to three frequencies sequentially. As three unknown variables (wind, temperature, and aerosol backscatter ratio) are involved in forming wind ratios, the three-frequency measurements allow one to derive S accurately. A least-square fit to the three wind ratios obtained in zenith direction at three predetermined frequencies, corresponding to absorption of the seed laser by the absorption line of 30%, 50%, and 70% on the I_2 line 1109, gives $\frac{dR_W}{d\nu}$ as the slope, and the midpoint wind ratio in zenith direction provides R_0 . The S is then calculated from Eq. (5). Based on the uniform sensitivity assumption mentioned above, the sensitivity S is identical in all directions; thus, the S measured in zenith direction can be applied to all off-zenith directions.

The retrieval method of LOS wind velocity described above is applicable to all measurement modes for this iodine-filter-based Doppler wind lidar. Because different modes deliver different final wind products, these measurement modes have different requirements on how precisely the three parameters ($R_{W,i}$, R_0 , and $dR_W/d\nu$) have to be determined experimentally. For example, the data retrievals for horizontal wind in wind profile mode and for the horizontal LOS wind in PPI mode cancel out the R_0 factor, and thus are immune to potential issues caused by the vertical wind assumption. Therefore, it is necessary to describe the retrieval methods of these major wind products as below.

1. Line-of-Sight Wind Velocity in Plan Position Indicator and Range Height Indicator Modes

The PPI is a well-known radar display that can show the distribution of LOS components of horizontal wind on a plane with a constant elevation. PPI scanning [29] is carried out with the apex of the scanning cone sitting at the lidar scanner, i.e., at a fixed elevation angle, the azimuth angle of the lidar beam is scanned through the entire 360 degrees. RHI scanning is used when the elevation of the lidar beam is varied to cover the majority of the upper hemisphere at a fixed azimuth direction. To illustrate the data retrieval procedure, a general flowchart including the procedure of LOS wind measurements in PPI and RHI modes is plotted in Fig. 5.

In the PPI mode, for a given range, the LOS wind ratio $R_{W,i}$ plotted as a function of azimuth angle shows a sinusoidal behavior (Fig. 6) in the ideal case of homogeneous atmosphere. This is because that the LOS wind velocity in the i th direction is given by

$$\begin{aligned} V_{\text{LOS},i} &= V_{\text{LOS},i,V} + V_{\text{LOS},i,H} \\ &= -V_V \sin \varphi + V_H \cos \varphi \cos \left[\frac{2\pi}{360} (\theta_i - \theta_0) \right], \end{aligned} \quad (7)$$

where $V_{\text{LOS},i,V}$ and $V_{\text{LOS},i,H}$ are the LOS wind components contributed by the vertical wind V_V and the horizontal wind V_H , respectively, to the i th LOS direction, φ is the elevation angle, θ_i is the azimuth angle in the i th direction (in degrees), clockwise from north, and θ_0 denotes the wind direction (in degrees). The linear relationship between R_W and V_{LOS} , mentioned earlier, leads to the wind ratio written as

$$R_{W,i} = R_V + \Delta R \cos \left[\frac{2\pi}{360} (\theta_i - \theta_0) \right], \quad (8)$$

where $R_{W,i}$ is the wind ratio measured at azimuth angle θ_i , R_V is the vertical-wind-induced wind ratio corresponding to the fitted DC offset, and ΔR is the wind ratio amplitude corresponding to the LOS wind of horizontal contributions.

To derive the LOS wind velocity from the measured wind ratio, we take the following steps. First, we measure the sensitivity slope $dR_W/d\nu$ in zenith direction with the lidar running at three frequencies sequentially as described above. Second, we conduct off-zenith PPI scans, and then fit Eq. (8) to the measured off-zenith wind ratios $R_{W,i}$ versus azimuth at each height to derive R_V and ΔR . An example of the fitting is shown in Fig. 6. Finally, the LOS wind velocity of horizontal contributions $V_{\text{LOS},i,H}$ at each azimuth angle is computed from $R_{W,i}$, R_V , and $dR_W/d\nu$ using Eq. (9), which is derived from Eq. (3):

$$V_{\text{LOS},i,H} = \frac{R_{W,i} - R_V}{3.76^* dR_W/d\nu} = \frac{\Delta R \cos \left[\frac{2\pi}{360} (\theta_i - \theta_0) \right]}{3.76^* dR_W/d\nu}. \quad (9)$$

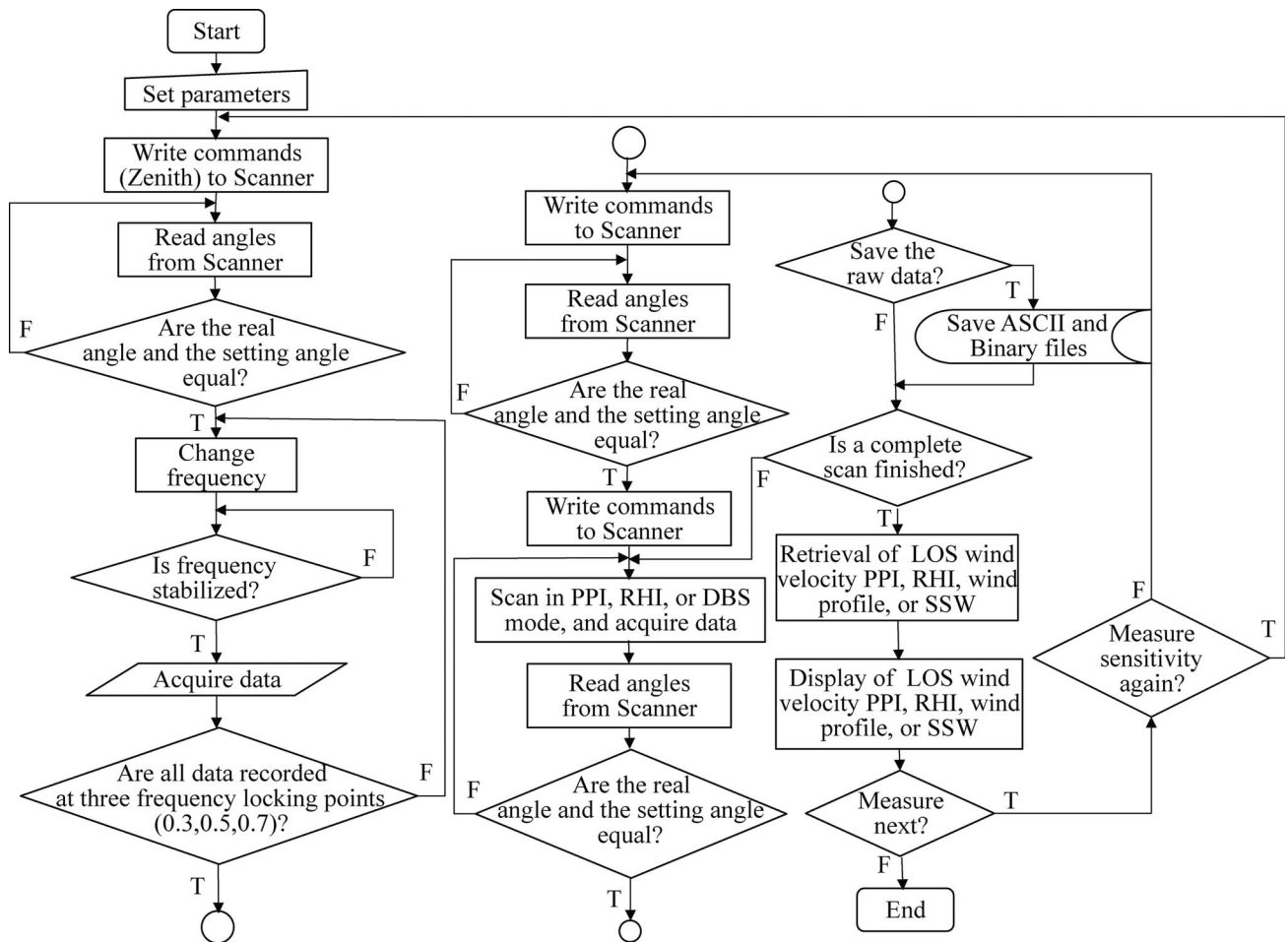


Fig. 5. General flowchart of all the products.

These LOS winds are then interpolated to a polar coordinate.

Equation (7) indicates that zero horizontal wind leads to zero amplitude of the sinusoidal curve, which provides an absolute wind calibration to horizontal winds. Furthermore, it is clear from Eq. (9) that in

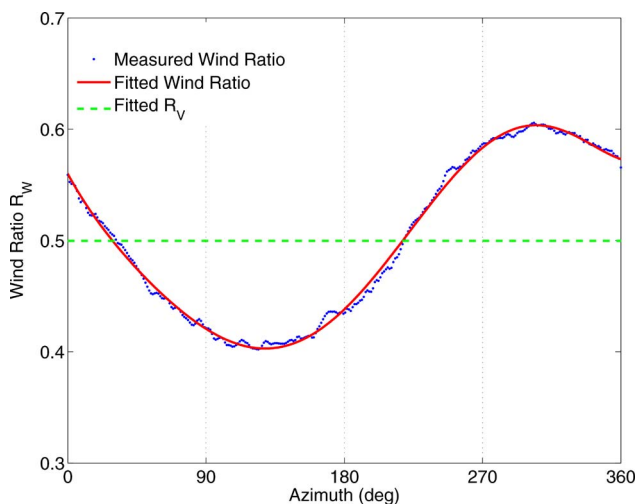


Fig. 6. (Color online) Example of wind ratio versus azimuth measured in PPI scan.

the PPI mode, the derived LOS winds of horizontal contributions are determined by the measured amplitude ΔR of the sinusoidal curve, independent of the zero-wind ratio R_0 . Thus, the LOS wind retrieval in PPI mode is not subject to the vertical wind assumption.

In the RHI mode, the wind ratio measured at zenith direction when the laser frequency is locked to the midpoint of the I_2 filter edge is taken as the zero-wind ratio R_0 . After we measure the sensitivity S in zenith direction as described above, V_{LOS} at each elevation angle of a RHI scan is calculated from Eq. (4) and then interpolated to a polar coordinate.

2. Wind Profile

The Doppler beam swing (DBS) technique [27] is applied to measure wind-altitude profiles, and rests on the assumption that the wind fields are horizontally homogeneous. By measuring the LOS wind velocities in four directions (east, west, south, north) and measuring the sensitivity in the zenith direction, we can derive the wind vector components (u , v , w) at the target altitudes. The flowchart plotted in Fig. 5 illustrates the procedure of wind profile measurement.

At a chosen elevation φ , the wind ratios obtained in five directions are given by

$$\begin{cases} R_{W,Z} = R_0 + \Delta R_V \\ R_{W,E} = R_0 + \Delta R_{H,E} + \Delta R_{V,E} \\ R_{W,W} = R_0 + \Delta R_{H,W} + \Delta R_{V,W}, \\ R_{W,S} = R_0 + \Delta R_{H,S} + \Delta R_{V,S} \\ R_{W,N} = R_0 + \Delta R_{H,N} + \Delta R_{V,N} \end{cases} \quad (10)$$

where the second subscripts, Z , E , W , S , and N represent the zenith, east, west, south, and north directions, while H and V denote the horizontal and vertical directions. Taking two opposite directions, east and west, for example, the vertical wind contributions $\Delta R_{V,E}$ and $\Delta R_{V,W}$ are equal, while the horizontal wind contributions $\Delta R_{H,E}$ and $\Delta R_{H,W}$ have the same absolute values but opposite signs. Thus, the vertical components and the factor R_0 are cancelled out when taking the difference between $R_{W,E}$ and $R_{W,W}$ as shown in

$$(R_{W,E} - R_{W,W})/2 = (\Delta R_{H,E} - \Delta R_{H,W})/2 = \Delta R_{H,E}. \quad (11)$$

The LOS wind velocity of horizontal contributions in the east-to-west direction can then be computed as

$$V_{\text{LOS},EW,H} = \frac{\Delta R_{H,E}}{3.76 \cdot dR_W/d\nu} = \frac{(R_{W,E} - R_{W,W})/2}{3.76 \cdot dR_W/d\nu}. \quad (12)$$

The zonal wind profile is given by

$$u = V_{H,EW} = V_{\text{LOS},EW,H} / \cos \varphi. \quad (13)$$

Similarly, we obtain the meridional wind profile as

$$v = V_{H,SN} = V_{\text{LOS},SN,H} / \cos \varphi. \quad (14)$$

Therefore, the horizontal wind speed and direction can be derived by Eq. (15) according to the trigonometric relationship

$$\begin{aligned} V_H &= \sqrt{u^2 + v^2} = \sqrt{V_{H,EW}^2 + V_{H,SN}^2}, \\ \theta_H &= \arctan(u/v) = \arctan(V_{H,EW}/V_{H,SN}), \end{aligned} \quad (15)$$

where the signs of $V_{H,EW}$ and $V_{H,SN}$ are used to determine the wind direction (θ_H) in the correct quadrant. Here we take the definition of wind direction used in the World Meteorological Organization (WMO). That is, $\theta_H = 0^\circ$ corresponds to the wind blowing from the north while 90° is for the wind blowing from the east.

Equation (12) indicates that zero horizontal wind results in zero $\Delta R_{H,E}$ and $\Delta R_{H,W}$, leading to $R_{W,E} = R_{W,W}$. This fact provides an absolute wind calibration to the horizontal wind retrieval; thus, the horizontal wind profiles are unaffected by the vertical wind assumption.

3. Sea Surface Wind (SSW)

A very attractive product of the Doppler lidar is the two- and three-dimensional (2D and 3D) wind field in clear air, which is essential to high-resolution weather forecasting. SSW is one of the examples. The procedure of SSW measurement can be found in Fig. 5.

To measure SSW, the lidar is scanned in low-elevation PPI mode. First we obtain R_0 and S by experimental measurements using the three- V_{LOS} method described in [30,31]. That is, the LOS wind velocities are measured in three directions spread evenly across a nearly horizontal sector of 120° , i.e., the adjacent azimuths are separated by 60° . According to Eq. (8) and under the vertical wind assumption,

$$R_{W,0^\circ} = R_0 + \Delta R \cos(\Delta\theta_0),$$

$$R_{W,\pm 60^\circ} = R_0 + \Delta R \cos(\Delta\theta_0 \pm 60^\circ).$$

Thus, R_0 can be derived from

$$R_0 = R_{W,+60^\circ} + R_{W,-60^\circ} - R_{W,0^\circ}$$

by recalling the trigonometric relationship that

$$\cos(\Delta\theta_0 + 60^\circ) + \cos(\Delta\theta_0 - 60^\circ) - \cos(\Delta\theta_0) = 0.$$

For the middle LOS direction, the laser is tuned to three preset frequencies, enabling the measurement of sensitivity S as described earlier. Assuming the sensitivity is the same for observation points with the same radius from the lidar, we can derive all LOS wind velocities V_{LOS} in this low-elevation plane using Eq. (4) within the scanned range. Then we derive the horizontal wind for each observation point from measured V_{LOS} using the approach illustrated in Fig. 7.

In the near-horizontal scan, the LOS wind velocities at azimuth θ , $\theta + \Delta\theta$, and $\theta - \Delta\theta$ are given by

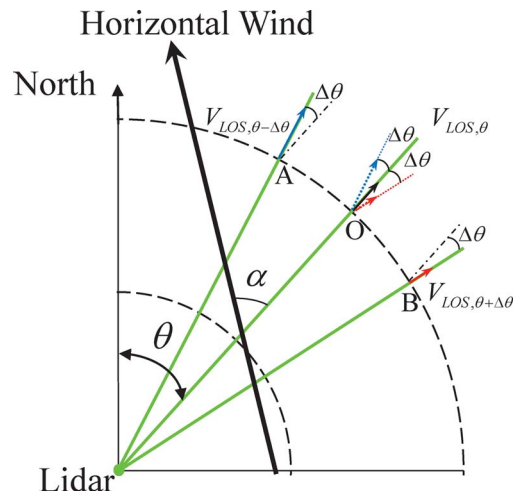


Fig. 7. (Color online) Schematic diagram of the sea surface wind retrieval method.

$$\begin{cases} V_{\text{LOS},\theta-\Delta\theta} = V_H \cos(\alpha - \Delta\theta) \\ V_{\text{LOS},\theta} = V_H \cos \alpha \\ V_{\text{LOS},\theta+\Delta\theta} = V_H \cos(\alpha + \Delta\theta) \end{cases}, \quad (16)$$

where α is the angle between wind direction and laser beam, V_H is the horizontal wind speed, $\Delta\theta$ is the azimuth interval. Under the assumption of local homogeneity, that is, the wind vectors at the same radius within small local area are uniform [30,31], the 2D wind field can be retrieved by Eq. (17) according to the trigonometric relationship. In other words, the angle α is calculated from two adjacent LOS wind velocities $V_{\text{LOS},\theta-\Delta\theta}$ and $V_{\text{LOS},\theta+\Delta\theta}$ using Eq. (17a), and then the horizontal wind is computed by Eq. (17b):

$$\alpha = \arctan\left(\frac{V_{\text{LOS},\theta-\Delta\theta} - V_{\text{LOS},\theta+\Delta\theta}}{V_{\text{LOS},\theta-\Delta\theta} + V_{\text{LOS},\theta+\Delta\theta}} \cdot \cot \Delta\theta\right), \quad (17a)$$

$$V_H = \frac{V_{\text{LOS},\theta}}{\cos \alpha}. \quad (17b)$$

The wind vectors derived for observation points were interpolated to the latitude and longitude grid points and displayed according to the criteria set by the Qingdao Meteorological Bureau. We first decompose the wind speed and wind direction of each observation point into the u and v weights. The u and v weights of each grid point are inversely proportional to the distance between the grid point and the observation points. The weight factor is larger for shorter distances, and vice versa. Assuming that u_i and v_i are the u and v values at an observation point, d_i is the distance between a grid point and the observation point, and M is the number of observation points that are used to calculate wind at one grid point, the u and v at this grid point can be derived as

$$\begin{cases} u = \sum_{i=1}^M (u_i/d_i) / \sum_{i=1}^M (1/d_i) \\ v = \sum_{i=1}^M (v_i/d_i) / \sum_{i=1}^M (1/d_i) \end{cases}. \quad (18)$$

Finally, we calculate the wind speed and the wind direction of each grid point based on the trigonometric relationship given by Eq. (15).

B. Error Analysis

As V_{LOS} is calculated from several measured variables using Eq. (6), three terms, R_W , R_0 , and $dR_W/d\nu$, contribute to the measurement errors of V_{LOS} . We first derive the general expression of the uncertainty ΔV_{LOS} to give the propagation of errors from R_W , R_0 , and $dR_W/d\nu$ to V_{LOS} , and then discuss the estimated errors resulting from various factors.

To derive the V_{LOS} measurement errors, we take the derivatives of Eq. (6)

$$\begin{aligned} \Delta V_{\text{LOS}} &= \frac{\partial V_{\text{LOS}}}{\partial R_W} \Delta R_W + \frac{\partial V_{\text{LOS}}}{\partial R_0} \Delta R_0 \\ &+ \frac{\partial V_{\text{LOS}}}{\partial (dR_W/d\nu)} \Delta (dR_W/d\nu), \end{aligned} \quad (19)$$

where ΔR_W , ΔR_0 , and $\Delta (dR_W/d\nu)$ represent the errors in the corresponding measured parameters, respectively. As the three error terms are not correlated and the partial derivatives on the right side of Eq. (19) can be easily derived from Eq. (6), the total root mean square (rms) LOS wind error is given by the error propagation

$$\begin{aligned} (\Delta V_{\text{LOS}})_{\text{rms}} &= \frac{1}{3.76^* (dR_W/d\nu)} \\ &\times \sqrt{(\Delta R_W)^2 + (\Delta R_0)^2 + [3.76 V_{\text{LOS}} \Delta (dR_W/d\nu)]^2}, \end{aligned} \quad (20)$$

The sources of errors can be classified into two categories. One is the uncertainties in measured R_W , R_0 , and $dR_W/d\nu$, mainly resulting from the photon noise of the return signals. The errors caused by these uncertainties are termed the “precision of wind measurements,” and are random errors. The other source is the biases, mainly caused by the deviations of our assumptions from the actual meteorological conditions in our case. The resulting errors are termed the “accuracy of measurements,” and are systematic errors. Here we discuss the precision and accuracy, respectively, of the lidar wind measurements.

With respect to the measurement precision, the photon-noise-induced random errors are estimated below for R_W , R_0 , and $dR_W/d\nu$. The wind ratio is given by $R_W = N_M/N_R$, where N_M and N_R are the signal photon counts of the measurement and reference channels, respectively. Following the derivation in [5] for photon noise and recognizing that the photon counts obey a Poisson distribution, the rms error of the wind ratio R_W is given by

$$\left(\frac{\Delta R_W}{R_W}\right)_{\text{rms}} = \frac{\sqrt{1 + \frac{1}{R_W}}}{\sqrt{N_R}} \sqrt{1 + \frac{2B_M + \frac{2B_R}{R_W^2}}{N_R \left(1 + \frac{1}{R_W}\right)}}, \quad (21)$$

where B_M and B_R are the background photon counts of the measurement and reference channels, respectively. As expected, the measurement errors decrease with increasing signal counts and decreasing background counts. The random error of R_0 can be derived in the same way as R_W , and the two error terms are similar: $(\Delta R_0)_{\text{rms}} \approx (\Delta R_W)_{\text{rms}}$. $dR_W/d\nu$ is determined through a linear fitting to the three-frequency measurements, as described in Subsection 4.A. The fitting significantly reduces the uncertainty of $dR_W/d\nu$, so the random error $[\Delta (dR_W/d\nu)]_{\text{rms}}$ is negligible in comparison to the other two terms. Therefore, the LOS wind measurement precision is estimated to be

$$(\Delta V_{\text{LOS}})_{\text{rms}} = \frac{\sqrt{2} \cdot (\Delta R_W)_{\text{rms}}}{3.76 \cdot (dR_W/d\nu)} \approx \frac{\sqrt{2}}{S} \cdot \left(\frac{\Delta R_W}{R_W} \right)_{\text{rms}} \quad (22)$$

An example of the LOS wind velocity is illustrated in the left panel of Fig. 8. The random errors computed according to Eq. (22), illustrated in the middle panel of Fig. 8, are less than 1 m/s below 5.5 km, increase with altitude as the signal levels decrease, and reach about 2.8 m/s at 8 km for an integration of 100 s. It is clear that the measurement precision is mainly determined by the signal-to-noise ratio (SNR) and the sensitivity S , as indicated by Eq. (22).

For the data retrieval methods described in Subsection 4.A, R_0 and $dR_W/d\nu$ are two parameters that must be determined experimentally under three assumptions (the horizontal homogeneity of atmosphere, the zero vertical wind, and the uniform sensitivity assumptions) mentioned above. Any deviations of the assumptions from the actual atmospheric conditions will result in bias in the measured R_0 , and $dR_W/d\nu$, thus affecting the accuracy of LOS wind retrieval. We examine the roles of these two terms in the data retrieval. Equation (6) can be rewritten as

$$V_{\text{LOS},i} = \frac{R_{W,i}}{3.76 \cdot dR_W/d\nu} - \frac{R_0}{3.76 \cdot dR_W/d\nu}.$$

Thus, it is clear that $dR_W/d\nu$ provides the proportional coefficient between V_{LOS} and R_W , while R_0 provides a “marker” for the zero wind calibration. Three unknowns (LOS wind, temperature, and aerosol backscatter ratio) are involved in the formation of the wind ratio; however, temperature and aerosol backscatter ratio no longer are included in our data retrieval equation. Therefore, R_0 and $dR_W/d\nu$ are the equivalent variants of these two unknown parameters. Using the three assumptions we made, R_0 and $dR_W/d\nu$ can now be measured in real time by pointing

the lidar beam to zenith direction and operating at three preset frequencies sequentially as discussed in Subsection 4.A. This data retrieval approach leads to real-time data retrieval without any model input. Such real-time and model-independent retrieval is an important capability in meteorological applications, and thus is the primary motivation for our data retrieval development. However, the validities of the three assumptions must be examined carefully in order to assess the applicable ranges of our approach.

The horizontal homogeneity of atmosphere is a good assumption for short integration periods and small scanned volume. As pointed out by Zhu *et al.* [32], the sensitivity is actually not uniform from zenith to off-zenith directions because the LOS wind velocity affects $dR_W/d\nu$. The systematic error of LOS wind due to the LOS-wind-induced changes of $dR_W/d\nu$ alone can be derived from Eq. (20) as

$$\Delta V_{\text{LOS}} = V_{\text{LOS}} \frac{\Delta(dR_W/d\nu)}{(dR_W/d\nu)}, \quad (23)$$

where $\Delta(dR_W/d\nu)$ is the deviation of the off-zenith sensitivity from the zenith sensitivity. It is clear that the wind bias is proportional to the percentage of the $dR_W/d\nu$ deviation and the LOS wind itself. As illustrated in [32], typical $\Delta(dR_W/d\nu)$ is negative, i.e., the sensitivity at $V_{\text{LOS}} = 0$ is larger than the sensitivity $V_{\text{LOS}} \neq 0$, so the retrieved V_{LOS} is biased towards smaller magnitudes. The sensitivity change with the LOS wind depends on the backscatter ratio $R_b = \beta_{\text{aer}}/\beta_{\text{mol}}$, where β_{aer} and β_{mol} are the backscatter coefficients of aerosols and molecules, respectively. When R_b is small (~ 0.1 or less), the relative deviation $\Delta(dR_W/d\nu)/(dR_W/d\nu)$ is also small ($\sim 3\%$) even for 20 m/s of LOS wind velocity. However, if R_b is larger than 0.5, then $\Delta(dR_W/d\nu)/(dR_W/d\nu)$ could be large ($>10\%$) if the LOS wind is over 10 m/s [32]. When the LOS wind is within ± 5 m/s, $\Delta(dR_W/d\nu)/(dR_W/d\nu)$ is no larger than 3%. The estimated bias for the

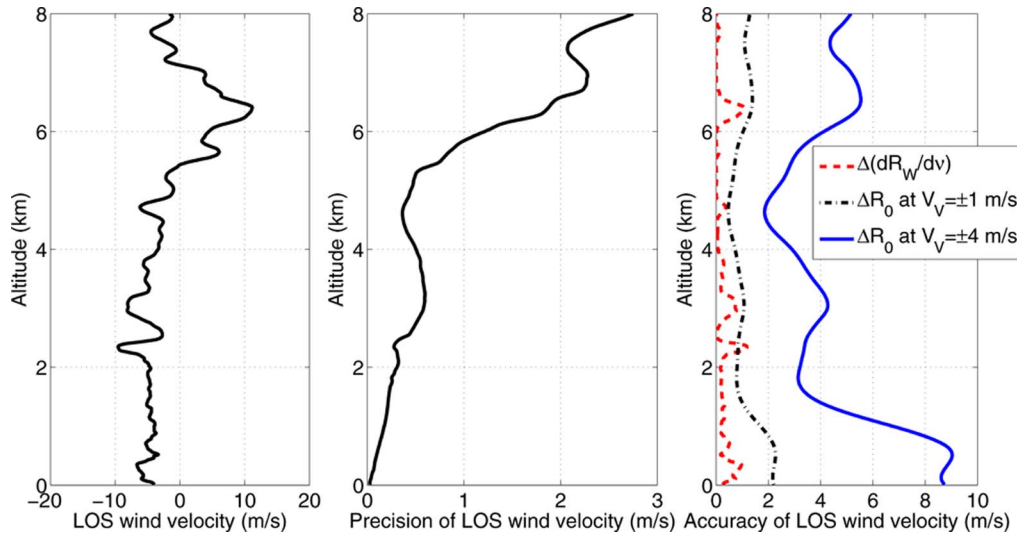


Fig. 8. (Color online) LOS wind velocity measured at azimuth of 90° (east) by the Doppler lidar at 22:09 LT on 4 March 2008, and the wind uncertainty under different vertical winds. The integration time $\Delta t = 100$ s and the spatial resolution $\Delta z = 10$ m.

example of LOS wind in Fig. 8 is illustrated as the dashed curve in the right panel of the figure. The R_b profile used in our error estimate is modeled to start with an initial value of 5 at ground, exponentially decayed to 0.1 around 2.5 km, and remaining at 0.1 throughout the higher altitudes. Through a similar simulation as carried out by Zhu *et al.* [32], the relative deviation $\Delta(dR_w/d\nu)/(dR_w/d\nu)$ was estimated and the wind bias was computed according to Eq. (23). The wind bias caused by the deviation $\Delta(dR_w/d\nu)$ was less than 1 m/s, comparable or smaller than the uncertainty caused by the photon noise shown in the middle panel of Fig. 8. Therefore, the uniform sensitivity assumption is applicable to the altitude range above the atmospheric boundary layers where R_b is nearly negligible if clouds are absent. It is also applicable to the range within the boundary layers if the LOS wind is less than 10 m/s.

The R_0 determination depends on the vertical wind assumption. Under quiet atmosphere conditions (e.g., nighttime), averaging over several minutes results in a vertical wind level close to zero, and our measurements in the zenith direction provide a good estimate of R_0 . However, under convective conditions within the atmospheric boundary layers, the vertical wind can deviate significantly from zero for considerable durations. Thus, the R_0 determination can be biased by the local vertical wind, introducing a systematic error to the LOS wind calibration. According to Eq. (20), the systematic error of LOS wind caused by R_0 alone is given by

$$\Delta V_{\text{LOS}} = \frac{\Delta R_0}{3.76 \cdot (dR_w/d\nu)} = \frac{1}{S} \cdot \frac{\Delta R_0}{R_0}, \quad (24)$$

where ΔR_0 is the deviation of measured R_0 from the real zero-wind ratio. This error could be significant if the local vertical wind is much larger than ± 1 m/s during the measurement period. We demonstrate this situation in the right panel of Fig. 8. If ΔR_0 is measured in zenith direction when the vertical wind $V_V = \pm 1$ m/s, the resulted LOS wind error is given by the dash-dotted curve in Fig. 8, ranging from ~ 1 m/s or less above the altitude of 2 km to about 2.5 m/s in the first 1 km of altitude. However, if the vertical wind is ± 4 m/s, then the error introduced by ΔR_0 will dominate the overall LOS wind error (shown as the solid curve), especially at the lower heights. R_0 and ΔR_0 are also dependent on R_b . Our simulation shows that larger R_b leads to larger ΔR_0 , thus to larger wind bias, for the same vertical wind deviation. In contrast to the situation of the sensitivity deviation, ΔR_0 could be either positive or negative, depending on the vertical wind deviation, and this also applies to the wind bias. The analysis we have presented here indicates that our data retrieval approach using R_0 and $dR_w/d\nu$ is not suitable for the convective conditions within atmospheric boundary layers. Based on our discussion of R_0 and $dR_w/d\nu$, this real-time and model-independent data retrieval approach is primarily applicable to altitudes above

the atmospheric boundary layers under quiet and clear atmosphere conditions. Within the boundary layers, this approach is only applicable when the LOS wind is small and the atmosphere is less convective.

It is worth pointing out that the horizontal wind measurements in the wind profile mode and the horizontal LOS winds in the PPI mode are free of the vertical wind issue. As analyzed in Subsections 4.A.1 and 4.A.2, the vertical wind terms and zero wind terms are cancelled out, and the homogeneous atmosphere assumption provides an absolute zero wind calibration to horizontal winds. Both horizontal winds, however, are still affected by the sensitivity measurements. The errors in laser central frequency and linewidth also affect the measurement accuracy and precision. As described in [24,25], the Doppler lidar incorporates a well-controlled and well-calibrated laser system and thus wind errors (much lower than 1 m/s) are well within the measurement precision and accuracy discussed above. Finally, since both R_0 and $dR_w/d\nu$ are functions of the aerosol backscatter ratio and temperature, our data retrieval methods rely on the horizontal homogeneity assumption of the atmosphere within the scanned volume and measurement periods.

5. Results

The incoherent Doppler wind lidar has been deployed in numerous campaigns, and a large amount of data has been collected. Here we highlight some key results to demonstrate the capability of the lidar and the data retrieval products.

A. Wind Profiles Measured by Doppler Beam Swing Scans

The measurement procedure of DBS for wind profiles has been illustrated in the general flowchart of Fig. 5. We start with the sensitivity measurements at zenith direction with the laser tuned to three frequencies as described earlier. Then the Doppler lidar beam is pointed off-zenith at an elevation of 60° and swung at four azimuth angles of east (90°), west (270°), south (180°), and north (0°) sequentially to measure the LOS wind velocities in these four directions. The zenith and off-zenith measurements form a complete data set for deriving wind profiles. The data are processed in near-real time and the retrieved wind profiles are displayed simultaneously. We then can choose either to move the lidar beam back to zenith to repeat the procedure, or to continue the off-zenith measurements, assuming the sensitivity unchanged, within an hour. The integration time for each frequency in zenith is 100 s, so it takes 5 min for the sensitivity measurements. We also integrate 100 s in each direction for the four azimuths. Adding the time to swing the beam, wind profiles are obtained with a temporal resolution of 15 min (or 10 min without the sensitivity measurement). Wind profile data are retrieved with a vertical resolution of 30 m.

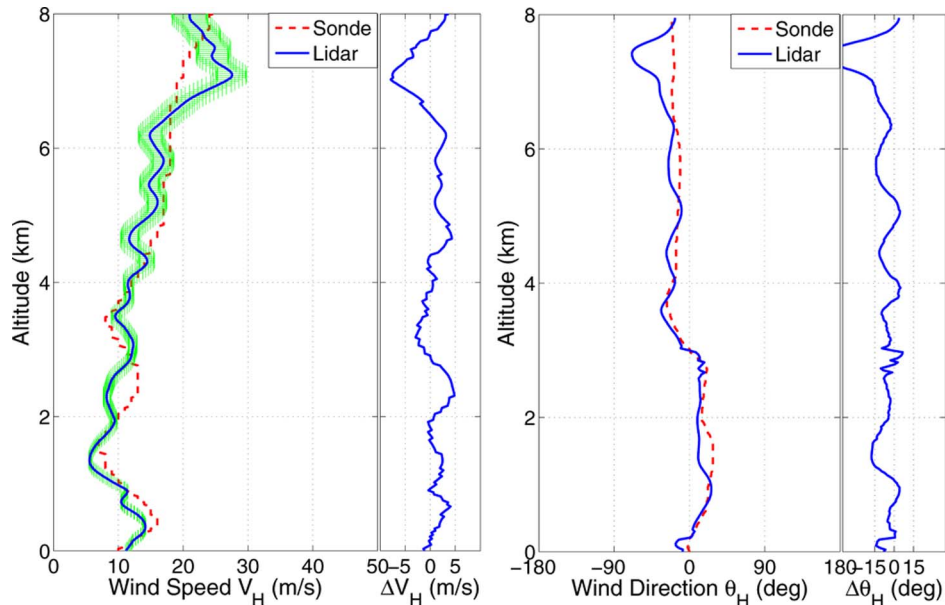


Fig. 9. (Color online) Horizontal wind profile measured by the Doppler lidar from 09:13 to 09:28 LT local time on 19 March 2008 is compared to the balloon sonde data taken at the same time. The spatial resolution is 30 m in order to compare with sonde. ΔV_H and $\Delta \theta_H$ represent the differences between the lidar and balloon data for the wind speed and direction, respectively.

Two examples of obtained wind profiles are plotted in Fig. 9 for daytime measurements, and in Fig. 10 for nighttime measurements. The lidar data (solid curves) are compared to the sonde data (dashed curves) of a balloon launched at the Qingdao Meteorological Station. The horizontal separation between this station and the lidar site at the Ocean University of China is 900 m. The error bars in Figs. 9 and 10 represent the wind measurement uncertainties caused by photon noise. The differences in wind speed and wind direction between the lidar and balloon data are, respectively, plotted as ΔV_H and $\Delta \theta_H$ in Figs. 9

and 10, in order to quantitatively assess the agreement between the two sensors. Figure 9 shows the horizontal wind speed on the left and the wind direction on the right, measured from 09:13 to 09:28 local time (LT) on 19 March 2008 in Qingdao, China. The wind was approximately northerly through the measurement altitudes, but slightly northeasterly below 3 km, and then shifting to northwesterly above. The measurement uncertainty was ~ 1 m/s below 3 km and increased to ~ 4 m/s at 6 km and ~ 8 m/s at 8 km. The wind profile (Fig. 10) measured by the DBS scan at 20:00 LT on 19 October

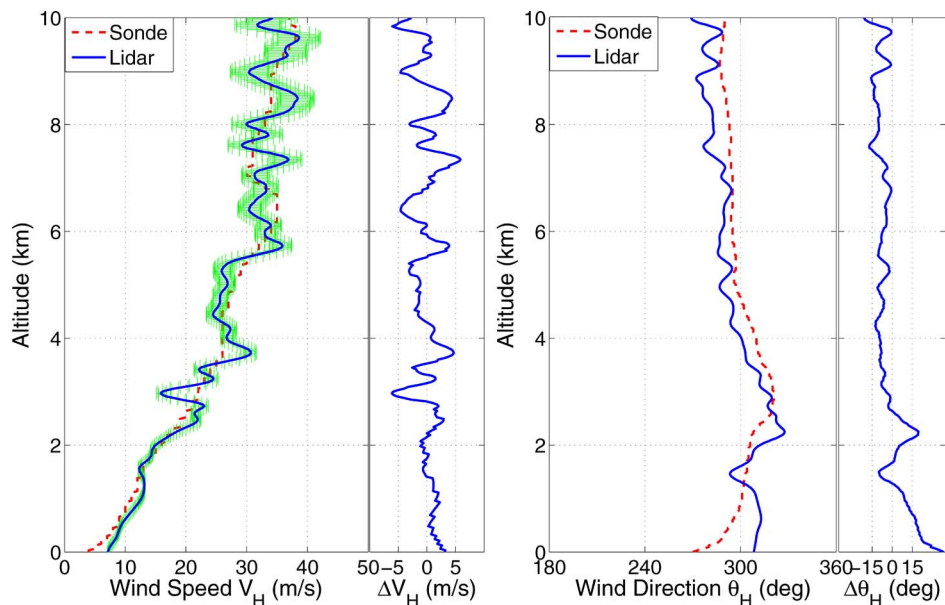


Fig. 10. (Color online) Horizontal wind profile measured by the Doppler lidar from 19:52 to 20:07 LT on 19 October 2007 is compared to the balloon sonde data taken at the same time. The spatial resolution is 30 m for both the lidar and the balloon data. ΔV_H and $\Delta \theta_H$ represent the differences between the lidar and balloon data for the wind speed and direction, respectively.

2007 indicated that the wind was northwesterly at the ground, and shifted to nearly westerly at altitudes above 5 km. The wind speed increased from 10 m/s at the surface to ~ 40 m/s near 10 km. The wind uncertainty was about 1 m/s below 3 km, and increased to ~ 8 m/s at 10 km.

The horizontal speed and direction of the wind obtained by the lidar generally agree well with those measured by the balloon at Qingdao. The rms differences in wind speed between the lidar and balloon data are computed to be 2.6 m/s and 2.3 m/s for the daytime and nighttime measurements, while the corresponding rms differences in wind direction are 10.7 deg and 10.2 deg, respectively. These results demonstrate that we can measure wind profiles accurately in clear atmosphere with the Doppler wind lidar. Such vertical profiles of wind speed and direction are valuable for applications including numerical weather forecasting models, rocket launch vehicle safety and load alleviation.

B. Line-of-Sight Wind Velocities Measured by Plan Position Indicator Scans

As illustrated in Fig. 5, the measurement procedure of PPI scans also starts with the sensitivity measurements at zenith direction by tuning the laser to three present frequencies. Then the lidar beam is pointed off-zenith to an elevation angle of 60° and scanned through the full azimuth of $0^\circ - 360^\circ$ with a constant angular speed of $2^\circ/\text{s}$. Thus, it takes 3 min for one full-azimuth scan. Such scanning can continue for as many cycles as specified by the user before returning to zenith to repeat the sensitivity measurements. During each full-azimuth scan, the DAAS reads the scanner's azimuth angle in real time, and integrates the lidar data over an interval of 2° , before saving one lidar profile to computer. After a full-azimuth scan is completed, the DAAS processes the data in real time to retrieve LOS wind velocities for 180 directions of LOS, as described in Subsection 4.A.1, and displays the results as a color contour in polar coordinates. Such LOS wind velocities are obtained and saved for each full-azimuth scan. As specified by the user, between two zenith sensitivity measurements, the results of new scans can be averaged with the previous results to produce a smoother color contour for better visual effects.

Examples shown in Fig. 11 demonstrate the LOS wind velocities measured by the PPI scans at a fixed elevation angle of 60° . The measurements were made at night, from 20:41 to 21:41 LT on 30 December 2007 in Qingdao, China. The radius in the plots represents altitude, with a maximum displayed altitude of 8 km, and white color denoting zero wind velocity. Duration of one full-azimuth scan in PPI mode is 3 min; the results are shown in Fig. 11(a) with a range resolution of 10 m. For the 180 directions, each LOS integrates for 1 s. Because of the high SNR, the measurement precision within 2.2 km appears to be high, even for this very short integration time. To visualize the wind fields better, we average 7 and 20 full-

azimuth scans and display them in Fig. 11(b) and 11(c), respectively. The zero wind line went from northeast to southwest below 3 km. The wind was northwesterly below 3 km, and shifted to westerly at 8 km. The wind speed increased sharply at about 7.5 km.

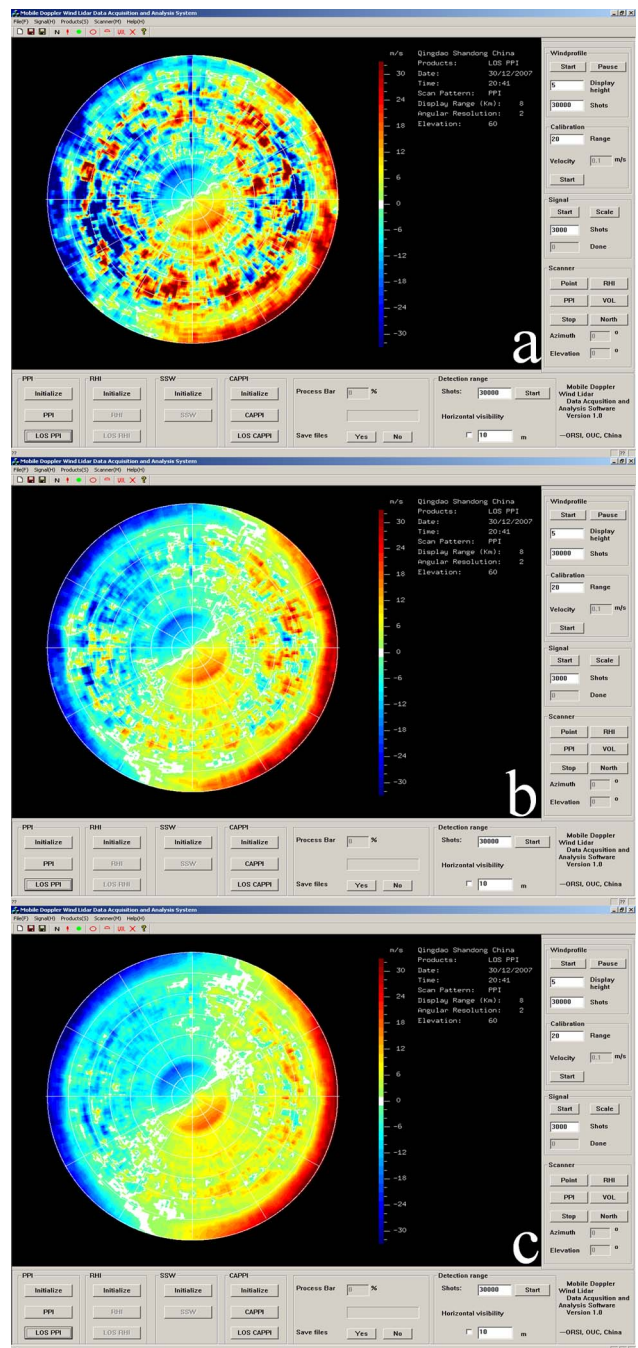


Fig. 11. (Color online) LOS wind velocity measured by PPI scans from 20:41 to 21:41 LT in the night on 30 December 2007. Color bar scales are from -33 to $+33$ m/s. White color denotes zero wind velocity. North is up, and east is to the right. Positive LOS wind velocity is defined as radially outward from the lidar. The radius in the plots represents the height, and the maximum displayed height is 8 km. Each circle is separated by 1.14 km. The spatial resolution $\Delta z = 10$ m, while the temporal resolutions are (a) $\Delta t = 3$ min, (b) $\Delta t = 21$ min, and (c) $\Delta t = 60$ min.

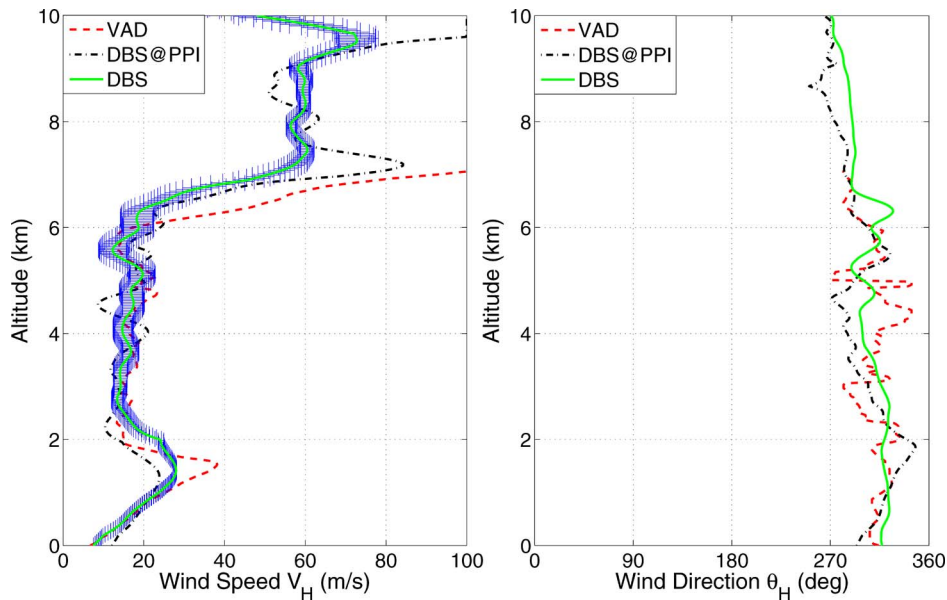


Fig. 12. (Color online) Wind profiles measured by the Doppler lidar in different scan modes with different data retrieval methods between 20:00 and 21:41 LT on 30 December 2007.

Figure 12 illustrates a comparison among three wind profiles obtained in different scan modes with different retrieval methods on 30 December 2007. The solid curve shows the wind profile with error bars, measured in DBS scan from 20:00 to 20:15 LT, with an elevation of 60° and retrieved by the method described in Subsection 4.A.2. The integration time is 100 s for each direction. The wind profile shown by the dot-dashed curve was also retrieved by the DBS method described in 4.A.2, but the data of the four azimuth directions (east, west, south, and north) were taken from the PPI scan (shown in Fig. 11). The integration time of each direction is 20 s. The wind profile shown by the dashed curve was derived from the PPI scan data shown in Fig. 11 using the velocity azimuth display (VAD) algorithm described in [27]. The integration time of each LOS direction is 20 s. As expected, the three wind profiles agree with each other quite well below 6 km where the VAD method has high SNR. The horizontal wind direction θ_H , as defined in Eq. (15), is shown in Fig. 12 and confirms the interpretation of Fig. 11. The comparison shows that the normal DBS scan provides the best measurements of wind profiles as it has larger detection range and higher SNR with higher temporal resolution.

The LOS wind velocities measured in PPI scans during daylight conditions are shown in Fig. 13. Again, one full-azimuth scan takes 3 min and Fig. 13 is an average of 8 full-azimuth scans with the data collected from 15:36 to 15:59 LT on 30 December 2007 in Qingdao, China at a fixed elevation of 60° . The PPI range scales extend from 0 to 8 km. The LOS velocity is plotted as color-shaded values between -33 and 33 m/s with positive defined as moving away from the lidar. Note the large apparent shear region to the ENE. The detection range of LOS wind velocity PPI reaches 8–10 km at night and 6–8 km during

the daytime. It is difficult to obtain LOS wind velocity PPI beyond these ranges due to the low SNR.

C. Line-of-Sight Wind Velocity Measured by Range Height Indicator Scans

The RHI scan is used to obtain altitude information about the LOS wind velocity in the direction of the predominant horizontal wind. The measurement procedure of RHI scan is similar to that of the PPI scan, except in RHI mode the azimuth angle is fixed and the elevation angle is scanned. In addition, the R_0 is obtained from the zenith beam. Examples of the LOS wind velocities measured by the RHI scans from 00:33 to 00:56 LT on 30 December 2007 in Qingdao,

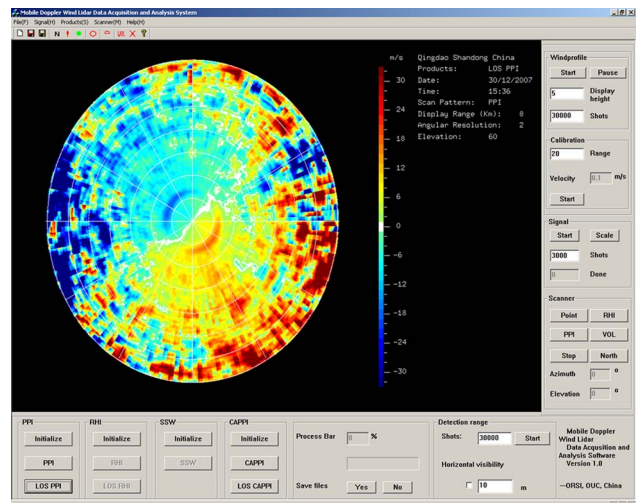


Fig. 13. (Color online) LOS wind velocity measured by PPI scan from 15:36 to 15:59 LT during daytime on 30 December 2007. The integration time is 8 s in each direction and the spatial resolution is 10 m. The radius in the plots represents the height, and the maximum displayed height is 8 km. Each circle is separated by 1.14 km.

China are displayed in Fig. 14. The RHI was produced at the azimuth of 0° and 180° with elevation scanned from 20° to 170° in a speed of $2^\circ/\text{s}$, stepped in 2° increments. Maximum measurement height was 8 km due to limited SNR. One full RHI scan takes about 100 s, and such a single-scan result is shown in Fig. 14(a). To visualize the wind fields better, Fig. 14(b) exhibits an average over 13 RHI scans.

The zero wind line shown as white color in Fig. 14 is along the zenith direction. A low velocity layer around 2.5 km to the south is clearly evident in the RHI display. The velocity below 2 km is about 15 m/s, decreases to 7–8 m/s between 2 km and 2.5 km, and increases to 13–14 m/s between 2.5 km and 3.5 km.

The PPI and RHI wind measurement capabilities demonstrated above with the incoherent Doppler

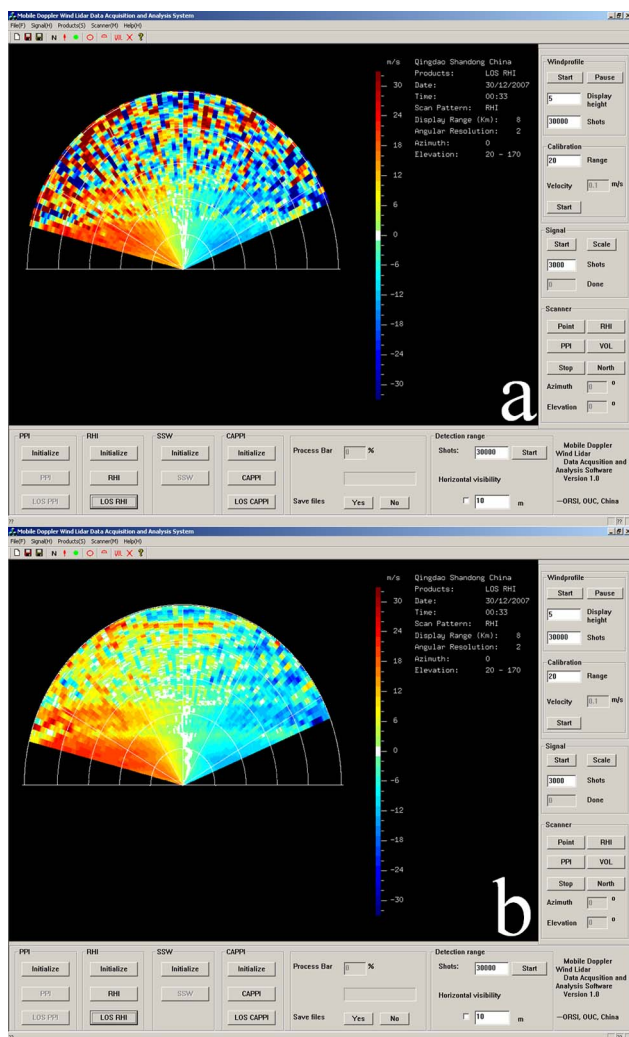


Fig. 14. (Color online) LOS wind velocity measured by RHI scans from 00:33 to 00:56 LT on 30 December 2007 in Qingdao, China. Color bar scales are from -33 to $+33$ m/s. North is to the right and positive LOS wind velocity is defined as radially outward from the lidar. The radius in the plots represents the height, and the maximum displayed height is 8 km. Each circle is separated by 1.6 km. The spatial resolution is 10 m, while the temporal resolutions are (a) 2 min and (b) 24 min.

lidar may have numerous applications. One of them is to monitor aircraft wing tip vortices generated by air flow over the wing [33]. Heavy aircrafts can generate very high-speed rotating flows that can remain for several minutes and can be very dangerous to other aircraft landing in similar areas within short intervals. These wake vortices may be detected by Doppler wind lidar in PPI or RHI modes when a higher scanning speed is used.

D. Sea Surface Wind Measured in 2008 Beijing Olympics

During a serial campaign in 2006 and 2007 [22], the incoherent Doppler lidar showed its capability in the near-horizontal wind measurements, due to its high pulse repetition rate, high scanning speed, and the sophisticated DAAS. Such near-horizontal wind measurements are very important to observe the inhomogeneous wind distribution in small scale. Based on these successful experiences, this mobile Doppler lidar was used to measure sea surface wind, providing meteorological service for the sailing competition during the 2008 Beijing Olympics from 8–22 August 2008 and for the 2008 Paralympics sailing competition from 8–13 September 2008 in Qingdao, China [23].

The measurement procedure of SSW is illustrated in the general flowchart of Fig. 5. The sector scan during the 2008 Olympics covered azimuth from 86° to 246° at an elevation of 1° . First, we measured R_0 at the azimuth of 106° and 226° , and measured the sensitivity S in the direction of 166° with the lidar running at three frequencies sequentially as described earlier. Then the horizontal wind speed and direction were derived from R_0 , S , and the measured wind ratio of each azimuth using the method described in Subsection 4.A.3. A full scan over the azimuth range of 160° was achieved in 160 s with a continuous azimuth scan speed of 1° per second. We averaged three or four adjacent LOS wind velocities, which resulted in 10 min averages, to achieve a

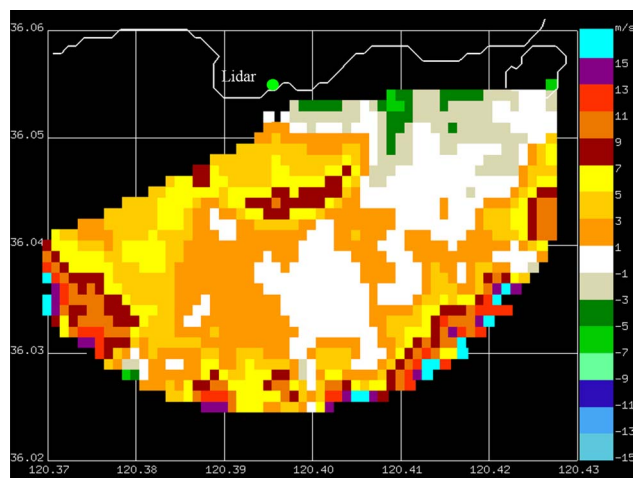


Fig. 15. (Color online) LOS wind velocity measured in sector PPI scan from 08:26 to 08:28 LT on 17 August 2008. The radius of scan is about 3 km, and the spatial resolution is 100 by 100 m. The x axis and y axis represent longitude (deg) and latitude (deg), respectively.

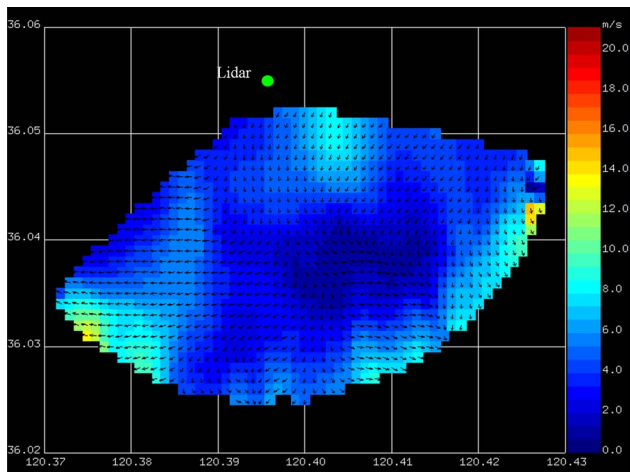


Fig. 16. (Color online) SSW measured from 08:26 to 08:28 LT on 17 August 2008. The radius of the scan is about 3 km, and the spatial resolution is 100 by 100 m. The x axis and y axis represent longitude (deg) and latitude (deg), respectively.

better SNR. More than 1000 LOS wind fields were obtained in a wide variety of conditions including both day and night operations. The detection range varied from 3 km to 8 km, depending on the atmospheric conditions. Figures 15 and 16 give examples of the measured LOS wind velocity PPI and SSW, respectively, from 08:26 to 08:28 LT on 17 August 2008. The colors indicate the wind speed and the arrows indicate the wind direction.

The high-resolution sea surface wind measurements are crucial for sailing regatta, but there is no instrument available so far to measure it except scanning Doppler wind lidar. The wind field measurement results were uploaded through a wireless network to the FTP server of Qingdao Meteorological Bureau for weather forecasts, with a period of 30 min for normal observations and a higher resolution of 10 min for critical applications. The data were used as the input parameters to the wind forecast models.

Based on the above measurement results and error analyses, we compare this incoherent Doppler lidar with current coherent Doppler lidars. Coherent lidars employ heterodyne detection of aerosol scattering signals. Since the local oscillator and frequency offset are accurately known, coherent lidars are in principle bias-free in wind measurements. The heterodyne detection technique is very efficient, leading to very high temporal resolution (several to tens of seconds) of wind measurements in the near-ground environment where the aerosols are abundant. However, it suffers low SNR at higher altitudes where the aerosol concentration is limited. Thus, the detection altitudes of coherent lidars are quite limited (~ 1 km) in relatively clear atmosphere when the concentration of aerosols is low. In contrast, the incoherent Doppler lidar presented in this paper relies on the iodine edge-filter technique and detects both molecular and aerosol backscatter signals. Hence, its detection range is much larger, even in clear atmospheric conditions.

The iodine edge filter used in the lidar receiver is inexpensive and well calibrated [18]. However, the detection principle results in a large portion of the return signal being blocked, leading to relatively low temporal resolution (\sim several minutes) when compared to coherent lidars in the aerosol abundant regions. Certainly, the temporal resolution can be significantly improved if higher laser power or larger receiver aperture is employed. Like other filter-based incoherent Doppler lidars, this Doppler lidar also faces issues of absolute wind calibration. High accuracy, however, can be obtained when extra frequency information and aerosol backscatter ratio are sought, as we will suggest in Section 6.

6. Conclusions and Outlook

A mobile Doppler wind lidar based on iodine filters has been developed at the Ocean University of China with full-azimuth-scan and full-elevation-scan capabilities as well as versatile measurement capabilities. An important feature of the lidar is its sophisticated and user-friendly Data Acquisition and Analysis System (DAAS), which allows wind measurements in various operation modes and data retrieval in real-time. The DAAS places the power of the Doppler wind lidar firmly in the hands of its users. This lidar has been deployed to measure wind profile, LOS wind velocity in PPI and RHI scans, and sea surface wind, etc., in numerous field campaigns. The detection range of LOS wind velocity in PPI and RHI modes can reach 8–10 km at night and 6–8 km during daytime with resolutions of 10 m and 3 min. The detection range of SSW varies from 3 km to 8 km, depending on the atmospheric conditions.

The incoherent mobile Doppler wind lidar offers opportunities for meteorological, environmental, and atmospheric research. It can also be utilized to detect and track aircraft wake vortices in PPI and RHI modes, detect wind shears around airports, and in wind field mode, provide wind field measurements during space shuttle landing. The wave structures shown in the RHI scans (Fig. 14) indicate the potential of such a lidar to detect atmospheric waves. In addition, this lidar has shown good potential for making 3D volume scans of the wind field. Combinations of various scan patterns, such as combining RHI with PPI scans, or RHI scans at several azimuth angles, would provide more information useful for local weather forecasts.

We have developed a set of data retrieval methods to process the lidar data of various operation modes for the LOS wind velocities and various final wind products. The basic approach is to retrieve the LOS wind velocity from the measured wind ratio utilizing the zero wind ratio and the sensitivity that are experimentally determined by pointing the lidar beam to zenith and operating at three preset frequencies sequentially. The advantage of this approach is to obtain high-resolution and real-time data retrieval without model input of temperature and aerosol backscatter ratio. However, the accuracy of this approach depends

on the validity of three assumptions (horizontal homogeneity of atmosphere, zero vertical wind, and uniform sensitivity) we made in the data retrieval, which leads us to conclude that this approach is limited to certain applicable ranges. Error analyses show that this approach is primarily applicable to altitudes above the atmospheric boundary layers under quiet atmosphere conditions (i.e., the averaged vertical wind is close to zero and the aerosol backscatter ratio is small). Within the boundary layers, this approach is only applicable if the LOS wind is small and the atmosphere is less convective. The horizontal wind measurements in the wind profile mode and the horizontal LOS winds in the PPI mode are free of the vertical wind issue because the vertical wind terms and zero wind terms are cancelled out. These data retrieval methods rely on the assumption of horizontal homogeneity of atmosphere that is a good approximation within a small scanned volume and short measurement periods.

Error analyses are useful in assessing the accuracy and precision of the lidar wind measurements. They also shed light on the potential improvements of this iodine-filter-based Doppler lidar. For example, if the three-frequency sensitivity measurements are performed for off-zenith LOS directions in the wind profile mode, then the sensitivity can be determined accurately even if local inhomogeneity occurs. This three-frequency technique will lead to the accurate determination of wind profiles. This accuracy improvement sacrifices the precision or temporal resolution to a certain degree if the laser power and receiver aperture remain the same. Furthermore, since both R_0 and $dR_w/d\nu$ strongly depend on the aerosol backscatter ratio R_b , it is beneficial to tune the lidar frequency to the bottom of the iodine absorption line occasionally to measure R_b in real time. Such a capability has been demonstrated by this lidar [34]. With proper algorithms, the information of R_b will help reduce the errors in the measurement accuracy. Finally, the correlation lidar technique that tracks distinct features of aerosols or clouds to deduce wind velocities may help to provide wind information in the cross LOS directions for the sea surface wind retrieval.

We sincerely acknowledge Professor Huang Li for his inspiration and advice in the development of DAAS. This work was supported by the National Natural Science Foundation of China (NSFC) grants 40427001 and 60578038, the China Meteorological Administration project *Mobile Doppler Lidar*, and the State Key Laboratory of Severe Weather, Chinese Academy of Meteorological Sciences project *Three-dimensional wind retrieval method based on single Doppler wind lidar*. Zhangjun Wang sincerely acknowledges the generous support from the China Scholarship Council for his study at the University of Colorado, Boulder. Xinzhao Chu and Zhangjun Wang were in part supported by the National Science Foundation (NSF) grants ATM-0545353 and ATM-0723229.

References

1. M. J. Post and R. E. Cupp, "Optimizing a pulsed Doppler lidar," *Appl. Opt.* **29**, 4145–4158 (1990).
2. R. M. Banta, L. S. Daray, J. D. Fast, J. O. Pinto, C. D. Whiteman, W. J. Shaw, and B. W. Orr, "Nocturnal low-level jet in a mountain basin complex. part I: Evolution and effects on local flows," *J. Appl. Meteorol.* **43**, 1348–1365 (2004).
3. C. J. Grund, R. M. Banta, J. L. George, J. N. Howell, M. J. Post, R. A. Richter, and A. M. Weichmann, "High-resolution Doppler lidar for boundary layer and cloud research," *J. Atmos. Ocean. Technol.* **18**, 376–393 (2001).
4. S. C. Tucker, W. A. Brewer, R. M. Banta, C. J. Senff, S. P. Sandberg, D. C. Law, A. N. Weickmann, and R. M. Hardesty, "Doppler lidar estimation of mixing height using turbulence, shear, and aerosol profiles," *J. Atmos. Ocean. Technol.* **26**, 673–688 (2009).
5. X. Z. Chu and G. C. Papen, "Resonance fluorescence lidar for measurements of the middle and upper atmosphere," in *Laser Remote Sensing*, T. Fujii and T. Fukuchi ed. (CRC Press, 2005) ISBN: 0-8247-4256-7, 179–432.
6. M. L. Chanin, A. Garnier, A. Hauchecorne, and J. Porteneuve, "A Doppler lidar for measuring winds in the middle atmosphere," *Geophys. Res. Lett.* **16**, 1273–1276 (1989).
7. B. M. Gentry and H. Chen, "Tropospheric wind measurements obtained with the Goddard Lidar Observatory for Winds (GLOW): validation and performance," presented at the International Symposium on Optical Science and Technology, San Diego, Calif., USA, 30–31 July 2001.
8. M. J. McGill, W. R. Skinner, and T. D. Irgang, "Validation of wind profiles measured using incoherent Doppler lidar," *Appl. Opt.* **36**, 1928–1939 (1997).
9. Y. Durand, A. Culoma, R. Meynart, D. Morancais, and F. Fabre, "Pre-development of a direct detection Doppler wind lidar for ADM/AELOUS mission," *Proc. SPIE* **5234**, 354–363 (2004).
10. J. A. McKay, "Assessment of a multibeam fizeau wedge interferometer for Doppler wind lidar," *Appl. Opt.* **41**, 1760–1767 (2002).
11. J. Q. Liu, J. Zhou, and W. B. Chen, "Boundary Doppler lidar based on multibeam Fizeau interferometer," *Proc. SPIE* **5653**, 273–280 (2005).
12. C. Flesia and C. L. Korb, "Theory of the double-edge molecular technique for Doppler lidar wind measurement," *Appl. Opt.* **38**, 432–440 (1999).
13. W. T. Huang, X. Z. Chu, B. P. Williams, S. D. Harrell, J. Wiig, and C. Y. She, "Na double-edge magneto-optic filter for Na lidar profiling of wind and temperature in the lower atmosphere," *Opt. Lett.* **34**, 199–201 (2009).
14. W. T. Huang, X. Z. Chu, J. Wiig, B. Tan, C. Yamashita, T. Yuan, J. Yue, S. D. Harrell, C. Y. She, B. P. Williams, J. S. Friedman, and R. M. Hardesty, "Field demonstration of simultaneous wind and temperature measurements from 5 to 50 km with a Na double-edgemagneto-optic filter in a multi-frequency Doppler lidar," *Opt. Lett.* **34**, 1552–1554 (2009).
15. J. S. Friedman, C. A. Tepley, P. A. Castleberg, and H. Roe, "Middle-atmospheric Doppler lidar using an iodine-vapor edge filter," *Opt. Lett.* **22**, 1648–1650 (1997).
16. C. A. Tepley, "Neutral winds of the middle atmosphere observed at Arecibo using a Doppler Rayleigh lidar," *J. Geophys. Res.* **99**, 25,781–25,790 (1994).
17. Z. S. Liu, W. B. Chen, T. L. Zhang, J. W. Hair, and C. Y. She, "An incoherent Doppler Lidar for ground-based atmospheric wind profiling," *Appl. Phys. B* **64**, 561–566 (1997).
18. Z. S. Liu, D. Wu, J. T. Liu, K. L. Zhang, W. B. Chen, X. Q. Song, J. W. Hair, and C.-Y. She, "Low-altitude atmospheric wind measurement from the combined Mie and Rayleigh backscattering by Doppler lidar with an iodine filter," *Appl. Opt.* **41**, 7079–7086 (2002).

19. C. Y. She, J. Yue, Z. A. Yan, J. W. Hair, J. J. Guo, S. H. Wu, and Z. S. Liu, "Direct-detection Doppler wind measurements with a Cabannes-Mie lidar: A. Comparison between iodine vapor filter and Fabry-Perot interferometer methods," *Appl. Opt.* **46**, 4434–4443 (2007).
20. C. Y. She, J. Yue, Z. A. Yan, J. W. Hair, J. J. Guo, S. H. Wu, and Z. S. Liu, "Direct-detection Doppler wind measurements with a Cabannes-Mie lidar: B. Impact of aerosol variation on iodine vapor filter methods," *Appl. Opt.* **46**, 4444–4454 (2007).
21. Z. S. Liu, B. Y. Liu, Z. G. Li, Z. A. Yan, S. H. Wu, and Z. B. Sun, "Wind measurements with incoherent Doppler lidar based on iodine filters at night and day," *Appl. Phys. B.* **88**, 327–335 (2007).
22. Z. S. Liu, B. Y. Liu, S. H. Wu, Z. G. Li, and Z. J. Wang, "A high spatial and temporal resolution mobile incoherent Doppler lidar for sea surface wind measurements," *Opt. Lett.* **33**, 1485–1487 (2008).
23. Z. S. Liu, Z. J. Wang, S. H. Wu, B. Y. Liu, Z. G. Li, X. Zhang, D. C. Bi, Y. B. Chen, R. Z. Li, and Y. Q. Yang, "Fine-measuring technique and application for sea surface wind by mobile Doppler wind lidar," *Opt. Eng.* **48**, 066002 (2009).
24. Z. S. Liu, S. H. Wu, and B. Y. Liu, "Seed injection and frequency locked Nd:YAG laser for direct-detection wind lidar," *Opt. Laser Technol.* **39**, 541–545 (2007).
25. S. H. Wu, Z. S. Liu, and B. Y. Liu, "Dual-wavelength laser frequency locking for the direct-detect wind lidar," *J. Mod. Opt.* **53**, 333–341 (2006).
26. Licel Ethernet Controller Installation and Reference Manual (Licel GmbH, 8 December 2005).
27. C. Werner, "Doppler wind lidar," in *Lidar: Range-resolved Optical Remote Sensing of the Atmosphere*, C. Weitkamp, ed. (Springer, 2005) ISBN 0-387-40075-3, 325–354.
28. B. M. Gentry, H. Chen, and S. X. Li, "Wind measurements with 355 nm molecular Doppler lidar," *Opt. Lett.* **25**, 1231–1233 (2000).
29. K. A. Browning and R. Wexler, "The determination of kinematic properties of a wind field using Doppler radar," *J. Appl. Meteorol.* **7**, 105–113 (1968).
30. Z. Y. Tao, "The VAP method to retrieve the wind vectors field based on single-Doppler velocity field," *Acta meteorol. Sinica* (In Chinese) **50**, 81–90 (1992).
31. C. Paulson, "The mathematical representation of wind speed and temperature profiles in the unstable atmospheric surface layer," *J. Appl. Meteorol.* **9**, 857–861 (1970).
32. J. S. Zhu, Y. B. Chen, Z. A. Yan, S. H. Wu, and Z. S. Liu, "Relationship between the aerosol scattering ratio and temperature of atmosphere and the sensitivity of a Doppler wind lidar with iodine filter," *Chinese Opt. Lett.* **6**, 449–453 (2008).
33. F. Köpp, S. Rahm, and I. Samlikho, "Characterization of aircraft wave vortices by 2 μm pulsed Doppler lidar," *J. Atmos. Ocean. Technol.* **21**, 194–206 (2004).
34. Z. G. Li, Z. S. Liu, Z. A. Yan, and J. J. Guo, "Research on characters of the marine atmospheric boundary layer structure and aerosol profiles by high spectral resolution lidar," *Opt. Eng.* **47**, 086001 (2008).